Multiscale Mechanics of Granular Biofilms

Lisa K. Månsson[1*], Anna E. Warsaw[2*], Elizabeth G. Wilbanks[2,3], Angela A. Pitenis[1]
[*] These authors contributed equally to this work and are designated as co-first authors.

[1] Materials Department
[2] Department of Ecology, Evolution, and Marine Biology
[3] Marine Science Institute
University of California, Santa Barbara, Santa Barbara, CA 93106

Abstract

Many hydrated and soft materials, including biological tissues and assemblies, permit fluid flow while retaining form and function. However, fundamental investigations of these complex materials are challenged by multiscale structural heterogeneity. Here, we characterized the structural and mechanical landscape of "pink berry" granular biofilms to determine the extent to which microscale heterogeneity influences macroscale material properties. We performed mechanical indentation measurements on intact granules as well as nanoindentation measurements on thin sections. We employed advanced imaging to correlate the internal structure and spatial organization of granules with quantitative measurements of their multiscale mechanical properties. We found that pink berries behave like soft (≈1 kPa), strain-rate dependent materials with fast relaxation times (≈1 s), indicating rapid transport of fluids with nutrients and other substances through the granule. Additionally, microscale mechanical measurements revealed individual contributions from the cell microcolonies and the extracellular matrix of the composite, summing to the observed macroscopic mechanical properties by applying the rule of mixtures based on structural composition obtained from imaging with fluorescence light sheet microscopy (≈34% cell microcolonies). This multiscale approach combining imaging and mechanics may be broadly applicable to investigations of other complex soft materials, from synthetic hydrogel composites to biologically heterogeneous spheroids, organoids, and tissues.

Keywords

biofilm matrix, extracellular polymeric substances, viscoelasticity, poroelasticity, indentation, light sheet microscopy

Corresponding Authors

Prof. Elizabeth G. Wilbanks
ewilbanks@ucsb.edu

Prof. Angela A. Pitenis
apitenis@ucsb.edu

1. Introduction

Multicellular life inherently depends on fluid flow to deliver nutrients that support growth and on the ability to hold together under diverse stressors. Light and electron microscopy indicate that these systems—from organoids to bacterial biofilms—exhibit intricate structural complexity spanning the nano- to macro-scales [1–3]. Nanomechanical measurements of single cells (e.g., atomic force microscopy) provide mechanobiological insights at the cellular and subcellular scale [4–12]. However, multicellular assemblies may exhibit different force responses to mechanical compression due to spatial heterogeneity and fluid flow [13].

Among the most ancient multicellular assemblies known to the living world are bacterial biofilms [14]. Mechanical measurements of bacterial biofilms relevant to both biomedical and industrial environments have typically focused on two-dimensional, laminar biofilms formed by single species [10–12, 15–26]. However, three-dimensional granular biofilms are also observed in both natural and engineered environments and play a critical role in industrial wastewater treatment technologies [27–30]. The mechanical properties of these granules are critical to their persistence in nature as well as their utility in industrial applications. Dense granules settle quickly which serves to retain catalytically valuable biomass within reactors, and rapid respiration depletes oxygen at the granule core, creating biofilms that can simultaneously catalyze both aerobic and anaerobic bioprocessing [27–30]. One of the few naturally evolved granular biofilms studied to date are the colorfully described “pink berry” microbial consortia [31]. Pink berries are pink-hued granules, often millimeters in diameter, found in intertidal salt marsh ponds (**Fig. 1**). Pink berries have enjoyed a long history of observation which has led to a genome-resolved understanding of the microbial community within the consortia [31–34]. Our prior work has established that these granules host diverse bacteria but are primarily composed of a single species of uncultivated phototrophic purple sulfur bacteria (*Thiohalocapsa* PSB1) which forms dense microcolonies within a translucent, supportive extracellular polymeric substances (EPS) matrix.

In this study, we present multiscale structure-property relationships of pink berry granular biofilms. We conducted in situ micromechanical measurements on intact granules as well as in situ nanomechanical measurements on thin sections to distinguish the respective contributions of

cell microcolonies and the EPS matrix to the mechanics of the composite. We leverage advanced imaging approaches to correlate granule structures and spatial organization with quantitative measurements of their mechanical properties.

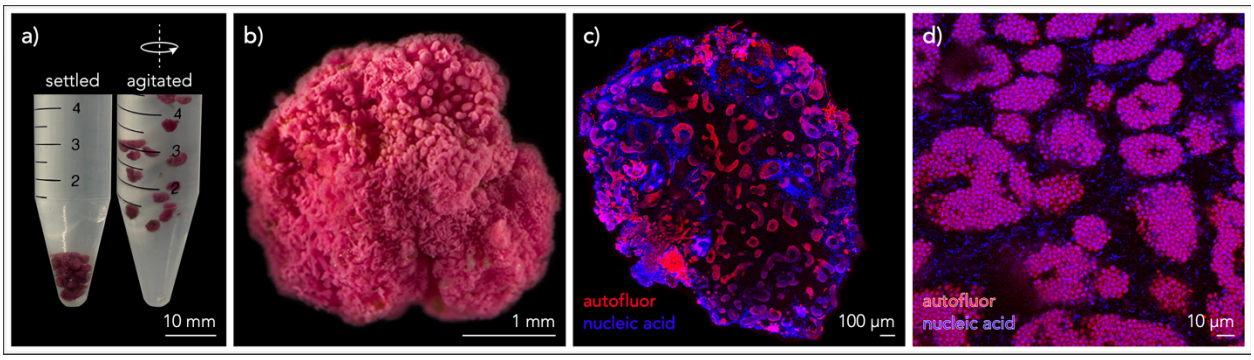

Figure 1: a) Pink berries settle quickly (left) and maintain integrity during agitation (right). b) Close-up view of a pink berry granular biofilm, reproduced from reference [34]. c) Fluorescence micrograph of a thin pink berry slice, with cells in blue (SYTO 41 Blue Fluorescent Nucleic Acid Stain) and cyanobacteria and purple sulfur bacteria (PSB) microcolony autofluorescence in red. d) Higher magnification view of PSB microcolonies in a pink berry slice, with cells in blue (DAPI) and PSB microcolony autofluorescence in red.

2. Materials and Methods

2.1. Sample Collection

Pink berry granular biofilms were sampled in September 2024 from an intertidal pond in the Little Sippewissett Salt Marsh in Falmouth, MA (N 41.57587, W -70.63923). Pink berry samples were collected with a sieve (1 mm mesh size) from the sediment-water interface, stored in water sampled from the site, and shipped to UC Santa Barbara. The pink berries were maintained as a concentrated collection in an aquarium with ≈3 cm sediment sampled from the site and about 6 L unfiltered seawater.

2.2. Microindentation of Pink Berries

Pink berries were collected from the aquarium and washed three times in 0.2 µm filter-sterilized seawater. The granular biofilms were positioned in a rigid transparent dish for unconfined compression while fully submerged in phosphate-buffered saline (PBS 3×) using a custom-built

microtribometer [35–41]. Pink berry deformation and recovery were recorded using an inverted digital microscope (Dino-Lite Edge AF4115ZT, 20–220× magnification) mounted beneath the dish. Pink berries were compressed at a constant approach and retraction velocity (v = 1, 10, or 100 µm/s) to a maximum applied normal force between F_N = 500 µN and 1 mN (contact pressures, P = 80 Pa to 330 Pa) using a hemispherical glass probe (radius of curvature, R_c = 2.6 mm) attached to a double-leaf cantilever (normal spring stiffness, K_N = 220 µN/µm). Each pink berry sample was indented at least three consecutive times (n = 3) with a minute in-between each indent to obtain the average elastic modulus at indentation velocities of v = 10 or 100 µm/s. Only one technical repeat (n = 1) was performed for the indentation velocity of v = 1 µm/s.

For calculation of reduced elastic modulus, E^*, the data were fit to the Hertzian contact mechanics model [42] using Eq. 1.

$$F_N = \frac{4}{3} E^* R_c^{\frac{1}{2}} d^{\frac{3}{2}} \#(1)$$

In this equation, F_N is the applied normal force, R_c is the hemispherical probe radius of curvature, and d is the microindentation depth. The energy absorbed, U_d, was calculated as the area between the loading and unloading curves, as previously reported [43–45].

2.3. Stress Relaxation Measurements

Pink berry samples were washed and positioned on a rigid dish for unconfined compression while fully submerged in PBS (3×) as described in Section 2.2. Using a cylindrical glass rod (radius, R_{cyl} = 0.75 mm), pink berry samples (N = 6) were compressed to an approximate strain of 5% at an approach velocity of v_{app} = 2 mm/s, held for 20 s, then retracted at v_{ret} = 0.05 mm/s (motion profile in **Fig. 3b**). The data was smoothed using a Savitzky-Golay filter in MATLAB, the force was normalized to the maximum force, and the characteristic stress relaxation time constant $\tau_{1/2}$ was determined at the time the force had decreased to half of its maximum value.

To extract diffusion coefficients from stress relaxation measurements, normalized normal force versus time data were fit to Eq. 2, which gives an expression for stress relaxation with a flat punch, described by Hu *et al.* [63].

$$(F - F_\infty)/(F_0 - F_\infty) = 1.304e^{-\sqrt{\tau}} - 0.304e^{-0.254\tau} \#(2)$$

In this equation, $\tau = (Dt)/R_{cyl}^2$, where D is the diffusion coefficient, t is time, and R_{cyl} is the cylindrical probe radius. In our case, F_∞ is the force after 19 s of relaxation, just before retraction of the probe after 20 s, and F_0 is the maximum compressive force.

2.3. Nanoindentation of Pink Berry Slices

To investigate the mechanical properties of subsurface features, pink berries were prepared for sectioning. A cylindrical disk of agarose was prepared by pipetting 4% (w/v) agarose gel in PBS (3×) in a rigid mold (≈20 mm diameter, ≈10 mm thickness). Prior to gelation of agarose at room temperature, a single pink berry was embedded live (unfixed) in the center of the mold. Thereafter, the cylindrical disk was sectioned on a Leica VT1000 S vibratome to obtain roughly 100 µm thick slices through the entire disk. Pink berry slices were stored in PBS (3×) in glass-bottom culture dishes at 4°C for up to one week prior to testing. During this time, negligible sample degradation was observed. To prepare slices for nanoindentation, a sterile glass-bottom culture dish was coated with 400 µL of Weaver's Gelatin (50 mL DI H_2O, 0.5 g chromium potassium sulfate dodecahydrate, 0.05 g gelatin type B) and equilibrated for 10 min at room temperature. The solution was aspirated, and the glass surface dried for 15 min at room temperature. Pink berry sections were gently patted dry with cellulose paper to remove excess liquid, positioned on the coated glass surface, and equilibrated for 20 min at room temperature. The culture dish was then filled with PBS (3×) for nanoindentation measurements. The full procedure is detailed in **Supplementary Fig. 1**.

Nanoindentation measurements were performed with the Optics11 Life Pavone housed in the BioPACIFIC MIP user facilities at UC Santa Barbara. Pink berry slices were indented at room temperature using a spherical glass probe (probe radius of curvature, R = 26.5 µm, normal spring

constant, K_N = 0.021 N/m) while fully submerged in PBS (3×) at a constant indentation velocity of v = 10 µm/s to an indentation depth of about 5 µm. Multiple positions across each slice (separated by at least two probe diameters) were selected using the inverted 20× objective installed in the instrument. Each position across the pink berry slice was indented at least three consecutive times in the same location to obtain average elastic modulus. All measurements were conducted at least two probe diameters from the perimeter of the pink berry, which is near the interface between the biofilm and the agarose gel matrix. The mechanical properties of the agarose support were characterized following the procedures above but with another probe (probe radius of curvature R = 48 µm, normal force spring constant K_N = 3.52 N/m) (agarose elastic modulus is about 500 kPa, **Supplementary Fig. 6**). Following nanoindentation measurements, pink berry slices were imaged to correlate multiscale mechanics with micro- to -macro-scale structure. Slices were imaged using an inverted Leica SP8 confocal microscope. A 10× (0.3 NA) air objective lens was combined with tile scanning to image entire pink berry slices. Brightfield images were acquired using 3×3 tiles with 10% overlap.

The reduced elastic modulus (E^*) and energy absorbed (U_d) were calculated for nanoindentation measurements as described above. Statistical analyses were performed in Python using the *scipy* package, specifically the function *mannwhitneyu* for performing a Mann-Whitney u-test, as the nanoindentation data from purple sulfur bacteria (PSB) microcolonies were not normally distributed.

2.5. Fluorescence Light Sheet Microscopy and Analysis

To examine the internal architecture of the pink berry granular biofilms, a pink berry collected from an intertidal pond in the Great Sippewissett Salt Marsh, Falmouth, MA (N 41.58618, W -70.64228) was fixed, optically cleared, and imaged on a light sheet microscope. Briefly, the pink berry was twice washed in 0.2 µm-filtered seawater, fixed in 4% PFA in PBS (1×) for 1 h agitated at 125 rpm at room temperature, washed three times in PBS (1×), and stored in PBS (1×) at 4 °C for about one week. The pink berry was incubated in 100% methanol for about 2 h, twice washed in PBS (1×), and incubated in 500 µL clearing reagent iCBiofilm-H2 (TCI AMERICA) diluted 4:1 with sterile water for about 7 h. The pink berry was embedded in 1% (w/v) agarose

gel in the 4:1 iCBiofilm-H2:water solution. The agarose gelled within the barrel of a 1 mL plastic disposable syringe modified with a wider inlet to reduce compressive strains on the pink berry during aspiration. The syringe was stored at 4°C in the 4:1 iCBiofilm-H2:water solution until imaging. The pink berry embedded in agarose was partially extruded from the syringe and positioned within the light sheet microscope prior to imaging.

Light sheet imaging was performed using the Zeiss Lightsheet Z.1 microscope housed in the NRI-MCDB shared facility using the 20× CLARITY lens (refractive index = 1.46) combined with tile scanning. We acquired a Z-stack through 844 µm of the pink berry (670 slices, Z-step = 1.26 µm), spanning roughly half of the granule. A 488 nm laser at 10% intensity was used to excite pink berry autofluorescence, emitting at 505–545 nm, and 3×4 tiles were imaged with 10% overlap. The tiles were stitched together in Fiji (ImageJ) using the stitching plugin Grid/Collection Stitching [46]. Image analysis was conducted using Imaris 10.2.0. Three surface categories were created from the Z-stack, capturing the intact pink berry surface, bright abiotic crystals, and individual PSB microcolonies. These surfaces were created using machine learning segmentation which trained an AI segmentation model. One of the surface categories captured bright crystals that appeared in the Z-stack as an artifact of the clearing protocol and was used to remove these from the images. The microcolony category primarily captured PSB microcolonies but also included a small number of potential cyanobacterial and *Rhodobacteraceae* microcolonies. The volumes computed from the pink berry and microcolony surfaces were used to calculate microcolony volume fraction.

3. Results

3.1. Pink Berry Granular Biofilms Exhibit Soft and Time-Dependent Mechanical Properties

Microindentation measurements of whole pink berries revealed strain-rate-dependent mechanical properties. Measurements were performed using the experimental configuration shown in **Fig. 2a**. A representative force-displacement curve shown in **Fig. 2b**, indicates paths of approach and retraction, as well as the energy absorbed (U_d) during the indentation (given by the area between the two paths). Granules exhibited a range of reduced elastic moduli of $1.1 < E^* < 5.5$ kPa, with an average value of $E^* = 2.7 \pm 1.5$ kPa (N = 7). These values of elastic

modulus were calculated from our analysis of the approach curve at v = 10 µm/s (**Fig. 2b** and **Supplementary Fig. 3**). The reduced moduli of granular pink berry biofilms are within the reported range for two-dimensional, lamellar biofilms which is between 17 Pa and 50 kPa [16]. For all low-strain indentation measurements (F_N < 800 µN), serial force-displacement curves overlaid and did not suggest significant plastic deformation or strain-stiffening (**Supplementary Fig. 2a)**. However, the energy absorbed during indentation decreased slightly between consecutive indentation measurements (**Supplementary Fig. 2b)**. Across multiple pink berry samples, the energy absorbed ranged from 16< U_d < 55 nJ with an average value of U_d =38 ± 14 nJ (N = 7) (**Supplementary Fig. 3)**. Energy dissipation is a common feature of other biofilms [48], and the values reported herein are within the same order of magnitude as other biological samples, including marine colonial tunicates [45].

We examined the extent to which strain rate influenced the elastic modulus of a single pink berry sample (N = 1) over decreasing indentation velocity: v = 100 µm/s (n=3), 10 µm/s (n=3), and 1 µm/s (n=1). Pink berry elastic modulus increases with increasing indentation velocity (**Fig. 2c)** which may suggest viscoelastic and/or poroelastic contributions to the mechanical properties [49–53, 26, 54].

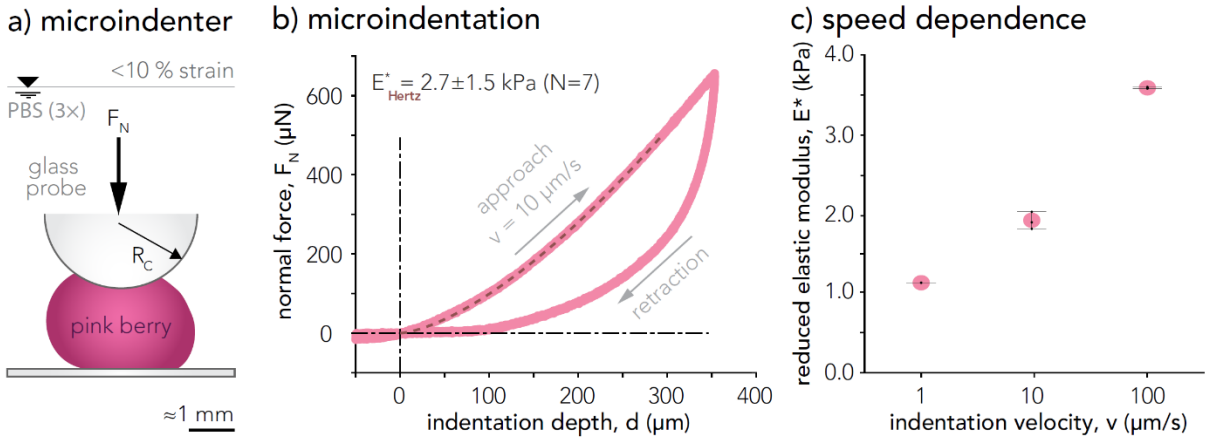

Figure 2: Microindentation measurements of whole pink berries. a) Experimental configuration for microindentation measurements. b) Representative force-displacement curve for a single pink berry sample with approach and retraction paths indicated. The Hertzian contact mechanics model (dashed line) was used to fit the approach curve to determine the elastic modulus, E^* = 2.7 ± 1.5 kPa (N = 7) (**Supplementary Fig. 3)**. c) Pink berry granular biofilms exhibit strain-dependent mechanical properties. Reduced elastic modulus plotted against indentation velocity (N=1; n = 3 for v = 10 and 100 µm/s, n = 1 for v = 1 µm/s).

3.2. Pink Berry Granular Biofilms Show Fast Response to Compression during Stress Relaxation

The custom-built microindenter was used to conduct stress relaxation measurements on individual pink berry granules. We modified the experimental configuration shown in **Fig. 2a** by using a cylindrical probe geometry and a different motion profile (**Fig. 3a,b**). Stress-relaxation measurements were plotted as force-time curves and normalized by the maximum force. The characteristic stress relaxation time, $\tau_{1/2}$, was determined as the time required for the applied force to reduce by half of its maximum value (**Fig. 3c**). For pink berry samples indented to an average strain of about 5% (N=6) pink berries, stress relaxation time scales $\tau_{1/2}$ were on the order of 0.1 to 10 s. The average stress-relaxation time was $\tau_{1/2} = 3.7 \pm 4.1$ s (N = 6) (**Fig. 3c** and **Supplementary Fig. 3**). Pink berry samples are thus considered 'fast-relaxing' compared to other biological and bioinspired samples, including tissues and hydrogels (**Fig. 3d**) [47, 55–59]; collagen biopolymers and heart tissues under modestly higher strains (10–15%) exhibit similar relaxation times [57, 59]. Interestingly, decellularized heart tissue is reported to relax more slowly compared to cellularized tissue [59]. The stress relaxation time differences reported between tissues with and without cells could indicate that contributions to the fast relaxation rates measured in pink berry samples may be partially due to the structure of bacterial microcolonies within the granule. Rheological stress relaxation studies of non-granular biofilms have reported characteristic time scales on the order of 100 to 1,000 s [51].

Pink berry samples contain high water content (≈70%); fluid flow through the pink berry granule may facilitate fast stress relaxation [17, 19]. Over the examined time scales herein, poroelastic responses may dominate [19, 60–62]. Stress relaxation measurements performed on alginate gels have been used by Hu *et al.* to infer material properties, including the diffusivity, D, and permeability, k [63]. Following this approach, we fit this poroelastic model to the stress-relaxation data to estimate the diffusion coefficient of pink berry samples, $D \sim 10^{-3}$ cm^2/s, with R^2-values between 0.6 to 0.9 for most fits (N = 5) (**Supplementary Fig. 4**). Disagreement between the poroelastic model and stress relaxation data may suggest additional viscoelastic contributions to pink berry stress relaxation that are unaccounted by the model. An additional consideration is the pink berry biofilm's complex composition and organization. However, the calculated diffusivity is generally similar to previously reported values for covalently-crosslinked

alginate gels, $D \sim 10^{-4}$ cm^2/s [63]. Together, our results suggest that the pink berry structure supports rapid transport of nutrients and other dissolved substances.

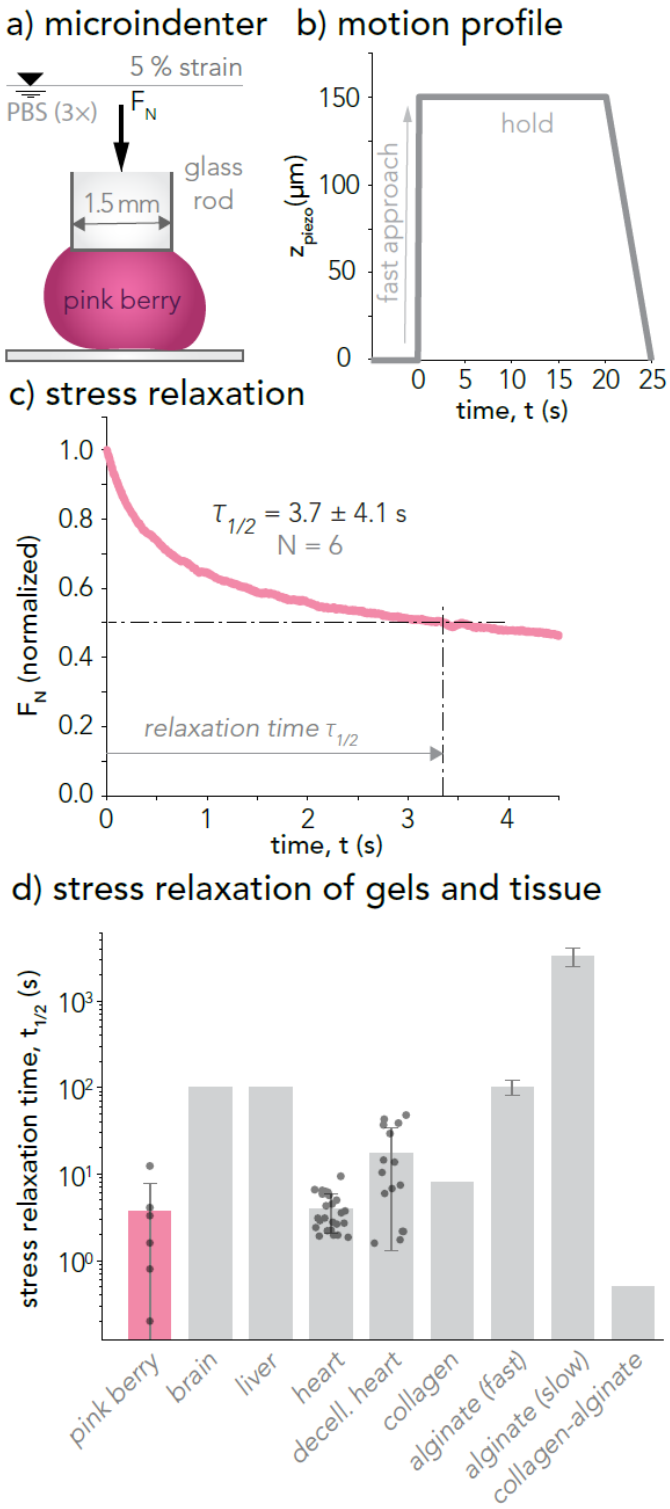

Figure 3: Pink berry granular biofilms exhibit fast relaxation during compression. a) Experimental configuration of stress-relaxation measurements. b) Microindenter motion profile.

c) Resulting stress relaxation curve from microindentation using the motion profile in b), where the normal force was normalized to the maximum force indented. Each pink berry was evaluated only once. d) Comparison of stress relaxation in pink berry granular biofilms to other tissue and common hydrogels [55–57, 59]. Bar height of average stress relaxation time computed from individual data points (circles); error bars represent the standard deviation.

3.4. Nanoindentations Reveal Microscopic Mechanical Heterogeneity in Pink Berries

To examine the microscale mechanical properties of the pink berry composite, we obtained thin sections of pink berry samples (about 100 µm thick). This sample thickness enabled nanoindentation measurements (**Fig. 4a**) on distinct constituents within the heterogenous pink berry structure. Nanoindentation measurements were conducted with an inverted 20× objective and a glass probe (R = 26.5 µm radius). Imaging through thin sections of pink berry enabled clear observations of purple sulfur bacteria (PSB) microcolonies embedded within extracellular polymeric substances (EPS) (**Fig. 4b**). The apparent contact area selected for each nanoindentation across the pink berry slice is shown by circles and the contact diameter, 2a, is indicated. The probe enabled sufficiently small contact areas to conduct nanoindentation measurements fully within either of the two major components of the pink berry (e.g. either microcolony or EPS domains) and minimized crosstalk.

Nanoindentation measurements revealed significant differences in reduced elastic modulus between PSB microcolonies (E^* = 2.1 ± 1.2 kPa, N = 2, n = 21) and the EPS matrix (E^* = 0.55 ± 0.13 kPa, N = 2, n = 30) (**Fig. 4c,d**). The reduced elastic modulus determined from nanoindentation measurements against PSB microcolonies ranged from E^* = 0.78 to 5.27 kPa, and from E^* = 0.35 to 0.8 kPa for the EPS matrix. The reported elastic modulus of the EPS matrix within pink berry granules are on the same order of magnitude as those determined from the EPS found in lamellar biofilms [66]. The average reduced elastic modulus between the PSB microcolonies and EPS matrix domains were determined to be statistically significant based on the Mann Whitney test (p-value = 0.000002).

Nanoindentation measurements revealed that PSB microcolonies absorbed significantly less energy than EPS matrix (p-value = 0.00037) (**Fig. 4e)**. The energy absorbed (U_d) by PSB microcolonies during nanoindentation ranged from 0.036 < U_d < 0.120 fJ with an average

reported value of U_d = 0.060 ± 0.02 fJ (N = 2, n = 21), while the EPS matrix exhibited energy absorption between 0.066 < U_d < 0.122 fJ with an average reported value of U_d = 0.093 ± 0.013 fJ (N = 2, n = 30). All tests were performed on two slices from the same pink berry. Image maps of whole pink berry slices with all positions measured together with each corresponding reduced elastic modulus value are presented in **Supplementary Fig. 5**.

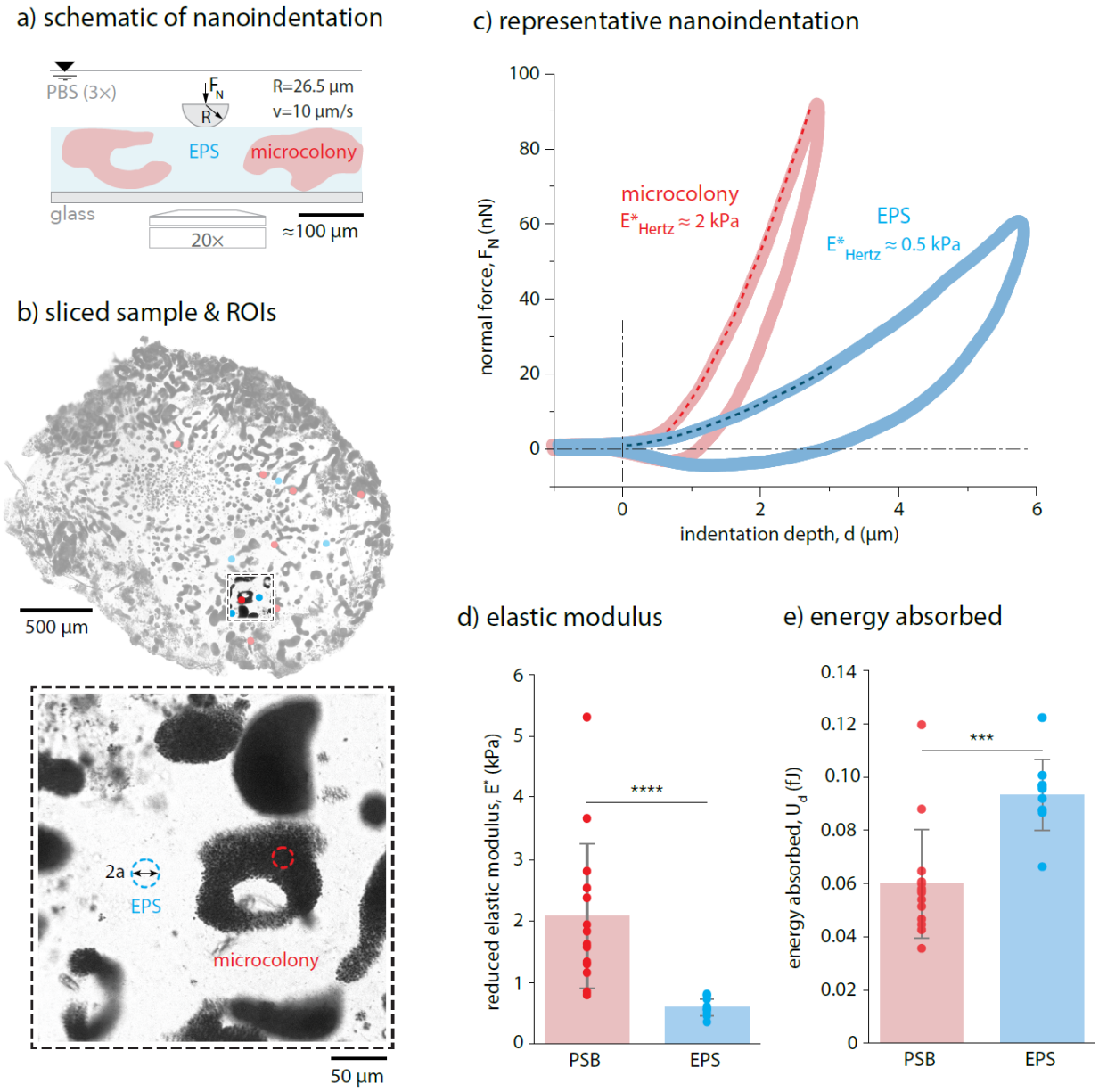

Figure 4: Nanoindentations of sliced pink berries reveal heterogeneity in mechanical properties at the micrometer scale. a) Schematic side view of experimental configuration. b) Brightfield image of the pink berry section, showing purple sulfur bacteria (PSB) (dark) and extracellular polymeric substance (EPS) (light) and probe contact radius, *a*, determined at maximum

indentation depth. c) Representative force-displacement curves from nanoindentation measurements in positions shown in b). Hertzian contact mechanics model (dashed lines) used to fit approach curves. d) PSB microcolonies exhibited higher elastic modulus but e) absorbed less energy than EPS.

3.5. High Resolution 3D Imaging Reveals Volume Fraction of Irregularly Shaped Microcolonies Distributed Throughout the EPS Matrix

To examine the internal structure of pink berry biofilms in 3D, we used fluorescence light sheet microscopy. While confocal microscopy is sufficient to obtain high resolution images of thin pink berry sections, to reconstruct the architecture of an entire granule with this method would require laborious serial sectioning and challenging merging of the subsequent Z-stack images. Light sheet microscopy, commonly used in neurobiology and developmental biology to image organs and embryos [67], images millimeter-sized samples with faster data acquisition and reduced photobleaching than confocal microscopy [68]. Using light-sheet microscopy, we imaged the internal architecture of an intact pink berry biofilm with single cell resolution (**Fig 5a**). Imaging revealed heterogenous, irregularly-shaped microcolonies distributed throughout the granule (**Fig. 5a**). The EPS matrix between microcolonies featured occasional diatoms (single-celled eukaryotic algae). A cropped region of the granule shows detail of microcolonies (**Fig. 5b**), which can be described as roughly tube shaped, ranging from 20–50 µm in diameter and 50–500 µm long, often curved and sometimes connected into a toroidal-like shape (**Fig. 5b,c**). Representative Z-slices through the 3D image show the spatial organization of PSB microcolonies as well as occasional bright masses of diatoms or cyanobacteria (e.g. in the upper center part of the second to last slice shown in **Fig. 5d**).

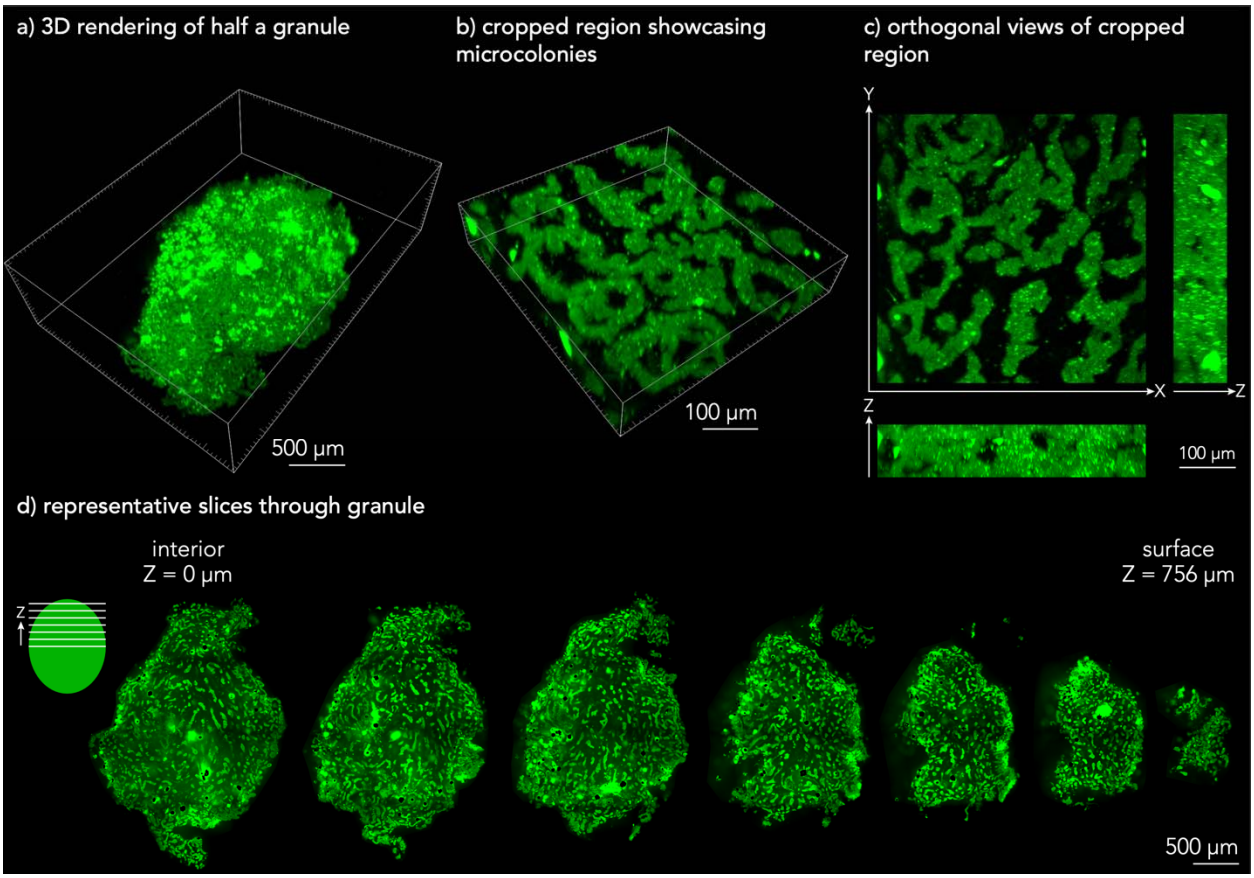

Figure 5: Light sheet microscopy reveals heterogeneous microcolonies distributed throughout the pink berry granular biofilm. a) Full 3D rendering of a Z-stack through half a pink berry granule. b) Cropped region of 3D rendering (500 × 500 × 100 µm) showcasing PSB microcolonies in green (autofluorescence). c) Orthogonal views of cropped region shown in b) in the XY, XZ, and YZ directions. d) Representative Z slices through Z-stack shown in a), from Z = 0 µm at the interior of the pink berry to Z = 756 µm near the surface. Each slice shown is 126 µm apart.

To further analyze pink berry composition, we used machine learning to obtain volumetric surface renderings capturing different components of the pink berry granular biofilm (**Fig. 6**). Using a surface reconstruction of the granule, we determined the volume to be 1.86×10^9 µm^3 (**Fig. 6a, 6b**). Surface reconstruction of each microcolony gave a summed microcolony volume of 6.29×10^8 µm^3 (**Fig. 6c, 6d**). In this granule, microcolonies corresponded to ≈34% of the pink berry volume and the EPS matrix made up ≈66% of the volume. Strikingly, linear combination of the nanoindentation moduli from these two components using the obtained volume fractions as weights (i.e., the rule of mixtures (Eq. 3) [69]) gives an estimate of the reduced elastic modulus of $E^*_{pink\ berry} =$ 1.1 kPa, which is in excellent agreement with the reduced elastic modulus determined from microindentation of the same pink berry, $E^* = 1.1 \pm 0.1$ kPa.

1

$$E^*_{\mathrm{EPS}} V_{EPS} + E^*_{\mathrm{PSB}} V_{PSB} = E^*{}_{pink\ berry} \#(3)$$

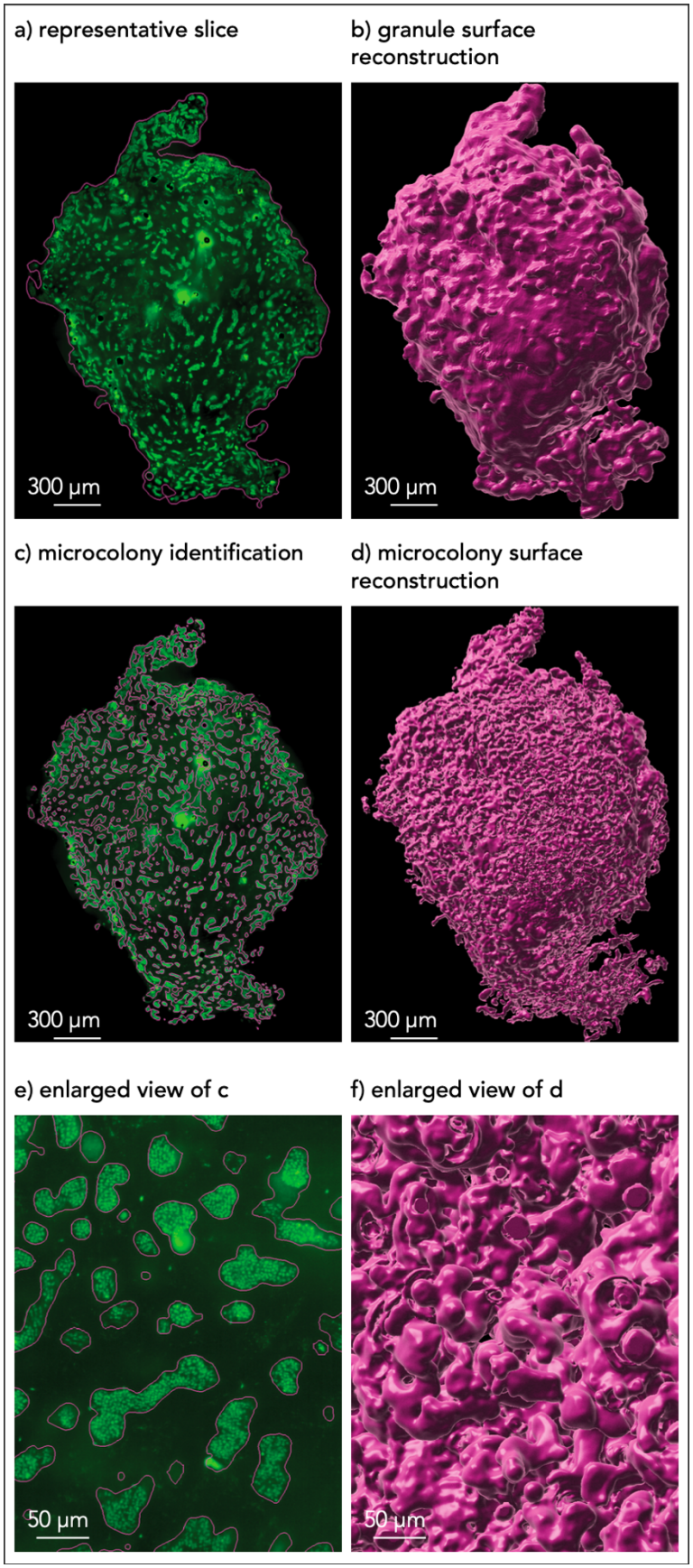
a) representative slice
b) granule surface reconstruction
300 µm
300 µm
c) microcolony identification
d) microcolony surface reconstruction
300 µm
300 µm
e) enlarged view of c
f) enlarged view of d
50 µm
50 µm

Figure 6: Microcolonies correspond to roughly 34% of the entire pink berry volume. a) Representative slice showing autofluorescent microcolonies (green) and the outline in pink representing the granule surface reconstruction shown in b. b) Granule surface reconstruction from a Z-stack through half a pink berry granule. Imaris was used to obtain the surface via machine learning segmentation. c) Representative slice illustrating autofluorescent microcolonies (green) and circled in pink is the microcolony surface rendering shown in d. d) Microcolony surface reconstruction from the same Z-stack using Imaris machine learning segmentation. e) Enlarged view of c to showcase microcolonies. f) Enlarged view of d.

4. Discussion

4.1 Methods Connecting Mechanical and Structural Characterization Across Length Scales

In this study, we present a set of methods to link multiscale mechanical properties to the visual landscape of composite biological samples. We performed mechanical measurements using indentation techniques across nN to µN forces and from nm to µm indentation depths. Advanced imaging techniques were performed to bridge the gap between smaller scale, high resolution imaging methods and larger scale visualization of entire macroscopic specimens. Light sheet fluorescence microscopy combined with tile scanning connected structural visualizations to the same length scales observed and measured for mechanical characterization. While more commonly used confocal microscopy enables optical sectioning, and thus 3D imaging, of samples at high resolution, light sheet microscopy imaged much deeper into samples, enabling imaging through entire intact granules [70]. Because this technique scanned a thin sheet of light across a sample (compared to the focused laser beam scanned across a sample in confocal imaging), light sheet imaging also results in much faster data acquisition with less photobleaching [68]. Light sheet fluorescence microscopy has been used to visualize structure and development of surface-attached biofilms [71, 72], but this study is the first of its kind to leverage light sheet microscopy to visualize the detailed 3D spatial organization of a granular biofilm at single-cell resolution.

This study examined the mechanical properties of the whole pink berry as well as the microscale constituents, including the PSB microcolonies and EPS matrix. The softer EPS matrix absorbs energy and maintains granule shape, preventing fracture under applied external stresses, while stiffer PSB microcolonies remain intact.

4.2 Estimating Permeability from Indentation

To gain insight into fluid permeability through pink berry biofilms, we calculated flow rate, Q, from the deformed volume, V_{deform}, schematically shown in **Supplementary Fig. 7**, divided by the indentation time t, as described in Eq. 4, where d_{max} is the maximum indentation depth and v is the indentation velocity. Thereafter, Q was used to derive an effective fluid permeability through the material, k.

$$Q = \frac{V_{\text{deform}}}{t} = \frac{V_{\text{deform}}\, v}{d_{\text{max}}} \#(4)$$

Fluid permeability describes fluid flow through a material in response to an applied pressure. Flow rate Q and the effective permeability k_{eff} can be related through the relationship in Eq. 5 [13], derived from Darcy's law:

$$k_{\text{eff}} = \frac{RhQ}{2E^{*}\pi a^{2}} \#(5)$$

In this equation, R is the probe radius of curvature, h is the sample thickness, E^{*} is the reduced elastic modulus, and a is the contact radius. From this relationship, permeability estimates can be calculated from both microindentation and nanoindentation measurements, respectively, presented in **Supplementary Fig. 8**.

For microindentation measurements of intact pink berry granular biofilms, the slowest indentation velocity, v = 1 µm/s, correlated with the lowest flow rate, $Q_{\text{micro}} = 2.5\times10^{-3}$ mm^3/s. The average flow rates estimated from nanoindentation measurements at v = 10 µm/s, were on the order of $Q_{\text{nano}} \sim 10^{-6}$ mm^3/s. We recognize the limitations in drawing direct comparisons between the mechanical properties determined from microindentations and nanoindentations, due to the differences between experimental configurations and limitations in motorized stage motion control. Despite these differences, we report estimates of permeability from both our microindentation and nanoindentation studies that are well-aligned with values reported across a

diverse variety of biopolymer networks and biological materials in the literature (**Supplementary Fig. 8**). From microindentation measurements, we report that the effective permeability of intact pink berry granules is between $k_{eff} = 10^{-15}$ and 10^{-13} m^2, and that it is strain rate dependent. Our nanoindentation measurements give permeability estimates of the PSB microcolonies and EPS matrix of $k_{eff} = 10^{-18}$ and 10^{-17} m^2 respectively. Further studies are warranted to better understand the sensitivity of permeability to strain rate at the nanoscale.

4.3 Relating Diffusivity to Permeability from Microscale Indentations

Our microscale stress-relaxation studies result in estimations of diffusivity, *D*, that we can relate to permeability, *k* through considerations of poroelasticity Eq. 6 [73].

$$k = \frac{(1-2v)}{2(1-v)}\frac{D\eta}{G} \#(6)$$

In this equation, the Poisson's ratio is assumed to be $v = 0.3$ [73, 74], the shear modulus, $G \sim E^*$ ~ 1 kPa, and the viscosity of water at room temperature is given by $\eta \approx 1$ mPa·s. From the calculated diffusivity, $D = 10^{-7}$ m^2/ s, we arrive at the estimated permeability of $k \approx 10^{-14}$ m^2, which is in good agreement with our estimations of *k* from pink berry indentations at 10 µm/s indentation speed. This simple analysis connects two different experimental techniques conducted on the same samples and the same instrument over the same force-, length-, and timescales.

4.4 Applications in Engineering

As a result of their functional construction, granular biofilms have recently gained increased attention in wastewater treatment technologies [29]. Microorganisms have been crucial in wastewater treatment since the turn of the 20th century with the advent of activated sludge, where microbes suspended in sewage help to break down organic matter. About 50 years ago, it was discovered that granular biofilms improved the wastewater treatment process. As

multispecies microbial assemblages with microbes spanning trophic groups, granular biofilms can break down more complex organic substances more completely. In addition, the densely-packed nature of granules protects microbes from stress in the surrounding environment and enables quick settling times, thus increasing biomass retention in flow-based systems. Altogether, granular biofilms promise a more efficient and reliable system.

As naturally occurring granular biofilms, pink berries have evolved over millenia to survive in their niche. Their microbial community composition, EPS matrix composition, and structural organization have been modified by nature, resulting in highly resilient structures capable of withstanding seasonal temperature variations and daily environmental variation in the highly dynamic salt marshes in which they are found. In terms of mechanical properties, they have balanced fluid flow, necessary for nutrient transport, with the ability to maintain structural integrity under external stresses.

In contrast to naturally occurring granules like pink berries, granular biofilms being used for wastewater treatment have been engineered in a bottom-up fashion. Microbes with functions of interest are combined in bioreactors to form granules, but the individual species have adapted separately to separate environments. By studying naturally occurring microbial granules like the pink berry, we can improve the design of engineered consortia for waste management technologies and beyond.

This study opens up opportunities for future work, such as investigations of extracted and decellularized EPS matrix for mechanical property separation as well as in the interest of soft biomaterials applications. The pink berry granular biofilm was used here as a model system for methods applicable across disciplines. We hope to inspire future work on other biomaterial systems and foresee a rich application space ranging from non-moldable synthetic materials to three-dimensional tissue-mimicking models like cancer spheroids and organoids.

4.5 Limitations

In this study, in situ indentation measurements enable the selection of regions of interest. However, our samples are generally layered such that they become opaque unless sectioned into very thin slices. Slices thinner than 100 µm presented significant experimental and handling challenges due to their fragility. Therefore, nanoindentations were performed using 100 µm thick sections, despite the uncertainty in knowing where in the Z plane PSB microcolonies were positioned. In contrast, EPS regions were translucent and easily discernible with available optics. The uncertainty in spatial positioning of the nanoindenter with respect to microcolony size, orientation, and distribution in the Z plane (normal to the sample holder) may explain the broad spread of E^* measurements associated with PSB microcolonies and the relatively more consistent results for EPS matrix measurements (**Fig. 4** and **Supplementary Fig. 5**). In situ measurements with live cell fluorescent reporters and confocal microscopy may overcome these experimental challenges.

While it would be ideal to conduct all imaging and mechanical analyses on the same pink berry samples, light sheet imaging requires fixation and optical clearing steps that would negatively impact subsequent mechanical characterization. For this reason, nanoindentations were not conducted on samples prepared for such imaging.

4.6 Future Work

The results presented here are a first approximation of the mechanical properties of pink berry granular biofilms. We believe there to be seasonal, geographical, and potentially day-night variability in properties like size and structure of the pink berries. Future studies will investigate variation in pink berry size, density, structure, and EPS matrix composition and explore how these variations impact mechanical properties of these biofilms. This work may help inform granule design and optimal environmental conditions in wastewater treatment systems.

Microscale variation in material properties throughout a granular biofilm can influence their macroscale properties and overall function. Radially symmetric density variation has been

observed in other granular biofilms, typically with a denser surface, and a less dense core [75]. EPS matrix variation, including composition and structured layering, have been found in other biofilms [76, 77]. While we did not find radially-symmetric trends from nanoindentations or imaging, a larger set of nanoindentation measurements positioned to investigate this property could improve our understanding of how spatial gradients influence function. Future studies will include investigation of EPS matrix composition and whether composition varies throughout the biofilms, as this could influence the mechanical properties of the composite.

5. Concluding Remarks

In this work, we have developed a sequence of methods bridging the gap between the visual and mechanical landscape across length scales of composite soft materials. Using the soft (~ 1 kPa) pink berry granular biofilm as a model system, we showed that this composite has strain-rate dependent mechanical properties and experience fast relaxation times (~ 1 s). Additionally, our methods revealed that by computing the structural composition of cell microcolonies (≈34%), we could relate individual microscale mechanical contributions from cell microcolonies and the extracellular matrix to the macroscopic properties crucial for pink berry biofilm function, including structural integrity and fluid transport. These complex yet compact biological systems have been heavily engineered by evolution, ready to inspire today's engineers. Continued investigation of the structural and mechanical properties of biological composites, ranging from biofilms to cancer spheroids, organoids, and beyond, will allow us to better understand nature and improve the built environment around us.

Conflicts of interest

The authors declare no conflict of interest.

Acknowledgements

We gratefully acknowledge the current and former members of the Interfacial Engineering Laboratory and the Wilbanks lab for helpful discussions. Special thanks to Dr. Benjamin Lopez for his assistance with light sheet imaging and image analysis. This work was primarily supported by the US Army Research Office under Cooperative Agreement No. W911NF-19-2-

0026 for the Institute for Collaborative Biotechnologies. We acknowledge the BioPACIFIC Materials Innovation Platform of the National Science Foundation (Award No. DMR-1933487) for the use of their shared user facilities, including the use of the Optics11 Life Pavone nanoindenter. We also acknowledge the use of the NRI-MCDB Microscopy Facility at UC Santa Barbara, including the Leica VT1000S vibratome, the Leica SP8 Resonant Scanning Confocal supported by the NSF MRI grant DBI-1625770 as well as the Zeiss Z.1 Lightsheet and Hercules computer workstation supported by the NIH Shared Instrumental Grant 1S10OD019969-01A1.

References

1. O'Toole G, Kaplan HB, Kolter R (2000) Biofilm Formation as Microbial Development. Annual Review of Microbiology 54:49–79. https://doi.org/10.1146/annurev.micro.54.1.49

2. Claessen D, Rozen DE, Kuipers OP, et al (2014) Bacterial solutions to multicellularity: a tale of biofilms, filaments and fruiting bodies. Nat Rev Microbiol 12:115–124. https://doi.org/10.1038/nrmicro3178

3. Mark Welch JL, Rossetti BJ, Rieken CW, et al (2016) Biogeography of a human oral microbiome at the micron scale. Proceedings of the National Academy of Sciences 113:E791–E800. https://doi.org/10.1073/pnas.1522149113

4. Chen CS (2008) Mechanotransduction – a field pulling together? Journal of Cell Science 121:3285–3292. https://doi.org/10.1242/jcs.023507

5. Tilghman RW, Cowan CR, Mih JD, et al (2010) Matrix Rigidity Regulates Cancer Cell Growth and Cellular Phenotype. PLoS One 5:e12905. https://doi.org/10.1371/journal.pone.0012905

6. Lu P, Weaver VM, Werb Z (2012) The extracellular matrix: A dynamic niche in cancer progression. J Cell Biol 196:395–406. https://doi.org/10.1083/jcb.201102147

7. Rice AJ, Cortes E, Lachowski D, et al (2017) Matrix stiffness induces epithelial–mesenchymal transition and promotes chemoresistance in pancreatic cancer cells. Oncogenesis 6:e352. https://doi.org/10.1038/oncsis.2017.54

8. Sarantis P, Koustas E, Papadimitropoulou A, et al (2020) Pancreatic ductal adenocarcinoma: Treatment hurdles, tumor microenvironment and immunotherapy. World J Gastrointest Oncol 12:173–181. https://doi.org/10.4251/wjgo.v12.i2.173

9. Liu J, Wu J (2024) The Pathogenesis and Impact of Arterial Stiffening in Hypertension: The 2023 John H. Laragh Research Award. American Journal of Hypertension 37:241–247. https://doi.org/10.1093/ajh/hpae006

10. Volle CB, Ferguson M, Aidala K, et al (2009) Physical Properties of Native Biofilm Cells Explored by Atomic Force Microscopy. Biophysical Journal 96:398a. https://doi.org/10.1016/j.bpj.2008.12.2025

11. James SA, Hilal N, Wright CJ (2017) Atomic force microscopy studies of bioprocess engineering surfaces – imaging, interactions and mechanical properties mediating bacterial adhesion. Biotechnology Journal 12:1600698. https://doi.org/10.1002/biot.201600698

12. Pattem J, Davrandi M, Aguayo S, et al (2018) A Multi-scale Biophysical Approach to Develop Structure-Property Relationships in Oral Biofilms. Sci Rep 8:5691. https://doi.org/10.1038/s41598-018-23798-1

13. Schulze KD, Zehnder SM, Urueña JM, et al (2017) Elastic modulus and hydraulic permeability of MDCK monolayers. Journal of Biomechanics 53:210–213. https://doi.org/10.1016/j.jbiomech.2017.01.016

14. Allwood AC, Walter MR, Kamber BS, et al (2006) Stromatolite reef from the Early Archaean era of Australia. Nature 441:714–718. https://doi.org/10.1038/nature04764

15. Wilking JN, Angelini TE, Seminara A, et al (2011) Biofilms as complex fluids. MRS Bulletin 36:385–391. https://doi.org/10.1557/mrs.2011.71

16. Böl M, Ehret ,Alexander E., Bolea Albero ,Antonio, et al (2013) Recent advances in mechanical characterisation of biofilm and their significance for material modelling. Critical Reviews in Biotechnology 33:145–171. https://doi.org/10.3109/07388551.2012.679250

17. He Y, Peterson BW, Jongsma MA, et al (2013) Stress Relaxation Analysis Facilitates a Quantitative Approach towards Antimicrobial Penetration into Biofilms. PLOS ONE 8:e63750. https://doi.org/10.1371/journal.pone.0063750

18. Safari A, Tukovic ,Zeljko, Walter ,Maik, et al (2015) Mechanical properties of a mature biofilm from a wastewater system: from microscale to macroscale level. Biofouling 31:651–664. https://doi.org/10.1080/08927014.2015.1075981

19. Peterson BW, He Y, Ren Y, et al (2015) Viscoelasticity of biofilms and their recalcitrance to mechanical and chemical challenges. FEMS Microbiol Rev 39:234–245. https://doi.org/10.1093/femsre/fuu008

20. Kundukad B, Seviour T, Liang Y, et al (2016) Mechanical properties of the superficial biofilm layer determine the architecture of biofilms. Soft Matter 12:5718–5726. https://doi.org/10.1039/C6SM00687F

21. Billings N, Birjiniuk A, Samad TS, et al (2015) Material properties of biofilms – key methods for understanding permeability and mechanics. Rep Prog Phys 78:036601. https://doi.org/10.1088/0034-4885/78/3/036601

22. Gordon VD, Davis-Fields M, Kovach K, Rodesney CA (2017) Biofilms and mechanics: a review of experimental techniques and findings. J Phys D: Appl Phys 50:223002. https://doi.org/10.1088/1361-6463/aa6b83

23. Gloag ES, Fabbri S, Wozniak DJ, Stoodley P (2020) Biofilm mechanics: Implications in infection and survival. Biofilm 2:100017. https://doi.org/10.1016/j.bioflm.2019.100017

24. Zhang Y, Young P, Traini D, et al (2023) Challenges and current advances in in vitro biofilm characterization. Biotechnology Journal 18:2300074. https://doi.org/10.1002/biot.202300074

25. Li M, Nahum Y, Matouš K, et al (2023) Effects of biofilm heterogeneity on the apparent mechanical properties obtained by shear rheometry. Biotechnology and Bioengineering 120:553–561. https://doi.org/10.1002/bit.28276

26. Wells MJ, Zhou X, Gordon VD (2024) Viscoelasticity of the Biofilm Matrix. In: Reichhardt C (ed) Biofilm Matrix. Springer Nature Switzerland, Cham, pp 259–282

27. Nicolella C, van Loosdrecht MCM, Heijnen JJ (2000) Wastewater treatment with particulate biofilm reactors. Journal of Biotechnology 80:1–33. https://doi.org/10.1016/S0168-1656(00)00229-7

28. Winkler M-KH, Meunier C, Henriet O, et al (2018) An integrative review of granular sludge for the biological removal of nutrients and recalcitrant organic matter from wastewater. Chemical Engineering Journal 336:489–502. https://doi.org/10.1016/j.cej.2017.12.026

29. Trego AC, Mills S, and Collins G (2021) Granular biofilms: Function, application, and new trends as model microbial communities. Critical Reviews in Environmental Science and Technology 51:1702–1725. https://doi.org/10.1080/10643389.2020.1769433

30. Rosa-Masegosa A, Rodriguez-Sanchez A, Gorrasi S, et al (2024) Microbial Ecology of Granular Biofilm Technologies for Wastewater Treatment: A Review. Microorganisms 12:433. https://doi.org/10.3390/microorganisms12030433

31. Seitz AP, Nielsen TH, Overmann J (1993) Physiology of purple sulfur bacteria forming macroscopic aggregates in Great Sippewissett Salt Marsh, Massachusetts. FEMS Microbiology Ecology 12:225–235. https://doi.org/10.1111/j.1574-6941.1993.tb00035.x

32. Wilbanks EG, Jaekel U, Salman V, et al (2014) Microscale sulfur cycling in the phototrophic pink berry consortia of the Sippewissett Salt Marsh. Environmental Microbiology 16:3398–3415. https://doi.org/10.1111/1462-2920.12388

33. Wilbanks EG, Doré H, Ashby MH, et al (2022) Metagenomic methylation patterns resolve bacterial genomes of unusual size and structural complexity. ISME J 16:1921–1931. https://doi.org/10.1038/s41396-022-01242-7

34. Doré H, Eisenberg AR, Junkins EN, et al (2024) Targeted hypermutation of putative antigen sensors in multicellular bacteria. Proc Natl Acad Sci USA 121:e2316469121. https://doi.org/10.1073/pnas.2316469121

35. Krick BA, Vail JR, Persson BNJ, Sawyer WG (2012) Optical In Situ Micro Tribometer for Analysis of Real Contact Area for Contact Mechanics, Adhesion, and Sliding Experiments. Tribol Lett 45:185–194. https://doi.org/10.1007/s11249-011-9870-y

36. Urueña JM, Hart SM, Hood DL, et al (2018) Considerations for Biotribometers: Cells, Gels, and Tissues. Tribol Lett 66:141. https://doi.org/10.1007/s11249-018-1094-y

37. Chau AL, Getty PT, Rhode AR, et al (2022) Superlubricity of pH-responsive hydrogels in extreme environments. Front Chem 10:. https://doi.org/10.3389/fchem.2022.891519

38. Chau AL, Edwards CER, Helgeson ME, Pitenis AA (2023) Designing Superlubricious Hydrogels from Spontaneous Peroxidation Gradients. ACS Appl Mater Interfaces 15:43075–43086. https://doi.org/10.1021/acsami.3c04636

39. Atkins DJ, Rosas JM, Månsson LK, et al (2024) Survival-Associated Cellular Response Maintained in Pancreatic Ductal Adenocarcinoma (PDAC) Switched Between Soft and Stiff 3D Microgel Culture. ACS Biomater Sci Eng 10:2177–2187. https://doi.org/10.1021/acsbiomaterials.3c01079

40. Rhode AR, Montes de Oca I, Chabinyc ML, et al (2024) Sliding on Slide-Ring Gels. Tribol Lett 72:121. https://doi.org/10.1007/s11249-024-01920-x

41. Atkins DJ, Rogers AE, Shaffer KE, et al (2025) Pro-Inflammatory Response to Macrotextured Silicone Implant Wear Debris. Tribol Lett 73:30. https://doi.org/10.1007/s11249-025-01965-6

42. Hertz H (1882) Ueber die Berührung fester elastischer Körper. Journal für die reine und angewandte Mathematik 92:156–171

43. Cappella B, Kaliappan SK, Sturm H (2005) Using AFM Force−Distance Curves To Study the Glass-to-Rubber Transition of Amorphous Polymers and Their Elastic−Plastic Properties as a Function of Temperature. Macromolecules 38:1874–1881. https://doi.org/10.1021/ma040135f

44. Mu Q, Cui K, Wang ZJ, et al (2022) Force-triggered rapid microstructure growth on hydrogel surface for on-demand functions. Nat Commun 13:6213. https://doi.org/10.1038/s41467-022-34044-8

45. Kwon Y, Singh S, Rodriguez D, et al (2023) Mechanical resilience of the sessile tunicate Botryllus schlosseri. Journal of Experimental Biology 226:jeb245124. https://doi.org/10.1242/jeb.245124

46. Preibisch S, Saalfeld S, Tomancak P (2009) Globally optimal stitching of tiled 3D microscopic image acquisitions. Bioinformatics 25:1463–1465. https://doi.org/10.1093/bioinformatics/btp184

47. Clark AH, Ross-Murphy SB (1985) The concentration dependence of biopolymer gel modulus. British Polymer Journal 17:164–168. https://doi.org/10.1002/pi.4980170214

48. Boudarel H, Mathias J-D, Blaysat B, Grédiac M (2018) Towards standardized mechanical characterization of microbial biofilms: analysis and critical review. npj Biofilms Microbiomes 4:17. https://doi.org/10.1038/s41522-018-0062-5

49. Stammen JA, Williams S, Ku DN, Guldberg RE (2001) Mechanical properties of a novel PVA hydrogel in shear and unconfined compression. Biomaterials 22:799–806. https://doi.org/10.1016/S0142-9612(00)00242-8

50. Klapper I, Rupp CJ, Cargo R, et al (2002) Viscoelastic fluid description of bacterial biofilm material properties. Biotechnology and Bioengineering 80:289–296. https://doi.org/10.1002/bit.10376

51. Shaw T, Winston M, Rupp CJ, et al (2004) Commonality of Elastic Relaxation Times in Biofilms. Phys Rev Lett 93:098102. https://doi.org/10.1103/PhysRevLett.93.098102

52. Di Stefano A, D'Aurizio E, Trubiani O, et al (2009) Viscoelastic properties of Staphylococcus aureus and Staphylococcus epidermidis mono-microbial biofilms. Microbial Biotechnology 2:634–641. https://doi.org/10.1111/j.1751-7915.2009.00120.x

53. Yang J, Shao C, Meng L (2019) Strain Rate-Dependent Viscoelasticity and Fracture Mechanics of Cellulose Nanofibril Composite Hydrogels. Langmuir 35:10542–10550. https://doi.org/10.1021/acs.langmuir.9b01532

54. Cuenot S, Fillaudeau A, Briolay T, et al (2025) Poroelastic and viscoelastic properties of soft materials determined from AFM force relaxation and force-distance curves. Journal of the Mechanical Behavior of Biomedical Materials 163:106865. https://doi.org/10.1016/j.jmbbm.2024.106865

55. Liu Z, Bilston L (2000) On the viscoelastic character of liver tissue: experiments and modelling of the linear behaviour. Biorheology 37:191–201

56. Lake SP, Hald ES, Barocas VH (2011) Collagen-Agarose Co-Gels as a Model for Collagen-Matrix Interaction in Soft Tissues Subjected to Indentation. J Biomed Mater Res A 99:507–515. https://doi.org/10.1002/jbm.a.33183

57. Chaudhuri O, Gu L, Klumpers D, et al (2016) Hydrogels with tunable stress relaxation regulate stem cell fate and activity. Nat Mater 15:326–334. https://doi.org/10.1038/nmat4489

58. Prouvé E, Drouin B, Chevallier P, et al (2021) Evaluating Poly(Acrylamide-co-Acrylic Acid) Hydrogels Stress Relaxation to Direct the Osteogenic Differentiation of Mesenchymal Stem Cells. Macromolecular Bioscience 21:2100069. https://doi.org/10.1002/mabi.202100069

59. Gionet-Gonzales M, Gathman G, Rosas J, et al (2025) Stress relaxation rates of myocardium from failing and non-failing hearts. Biomech Model Mechanobiol 24:265–280. https://doi.org/10.1007/s10237-024-01909-4

60. Biot MA (1941) General Theory of Three□Dimensional Consolidation. Journal of Applied Physics 12:155–164. https://doi.org/10.1063/1.1712886

61. Galli M, Comley KSC, Shean TAV, Oyen ML (2009) Viscoelastic and poroelastic mechanical characterization of hydrated gels. Journal of Materials Research 24:973–979. https://doi.org/10.1557/jmr.2009.0129

62. Hu Y, Suo Z (2012) Viscoelasticity and poroelasticity in elastomeric gels. Acta Mechanica Solida Sinica 25:441–458. https://doi.org/10.1016/S0894-9166(12)60039-1

63. Hu Y, Zhao X, Vlassak JJ, Suo Z (2010) Using indentation to characterize the poroelasticity of gels. Applied Physics Letters 96:121904. https://doi.org/10.1063/1.3370354

64. Urueña JM, Pitenis AA, Nixon RM, et al (2015) Mesh Size Control of Polymer Fluctuation Lubrication in Gemini Hydrogels. Biotribology 1–2:24–29. https://doi.org/10.1016/j.biotri.2015.03.001

65. Reale ER, Dunn AC (2017) Poroelasticity-driven lubrication in hydrogel interfaces. Soft Matter 13:428–435. https://doi.org/10.1039/C6SM02111E

66. Wloka M, Rehage H, Flemming H-C, Wingender J (2004) Rheological properties of viscoelastic biofilm extracellular polymeric substances and comparison to the behavior of calcium alginate gels. Colloid Polym Sci 282:1067–1076. https://doi.org/10.1007/s00396-003-1033-8

67. Chatterjee K, Pratiwi FW, Wu FCM, et al (2018) Recent Progress in Light Sheet Microscopy for Biological Applications. Appl Spectrosc, AS 72:1137–1169

68. Santi PA (2011) Light Sheet Fluorescence Microscopy: A Review. J Histochem Cytochem 59:129–138. https://doi.org/10.1369/0022155410394857

69. Jones RM (2018) Mechanics Of Composite Materials, 2nd ed. CRC Press, Boca Raton

70. Lazzari G, Vinciguerra D, Balasso A, et al (2019) Light sheet fluorescence microscopy *versus* confocal microscopy: in quest of a suitable tool to assess drug and nanomedicine penetration into multicellular tumor spheroids. European Journal of Pharmaceutics and Biopharmaceutics 142:195–203. https://doi.org/10.1016/j.ejpb.2019.06.019

71. Zhang J, Zhang M, Wang Y, et al (2021) Optically Accessible Microfluidic Flow Channels for Noninvasive High-Resolution Biofilm Imaging Using Lattice Light Sheet Microscopy. J Phys Chem B 125:12187–12196. https://doi.org/10.1021/acs.jpcb.1c07759

72. Šmerdová L, Füzik T, Valentová L, et al (2024) Dynamics of bacterial biofilm development imaged using light sheet fluorescence microscopy. 2024.07.10.602771

73. He D, Malu D, Hu Y (2024) A Comprehensive Review of Indentation of Gels and Soft Biological Materials. Applied Mechanics Reviews 76:. https://doi.org/10.1115/1.4065434

74. Lopez-Sanchez P, Rincon M, Wang D, et al (2014) Micromechanics and Poroelasticity of Hydrated Cellulose Networks. Biomacromolecules 15:2274–2284. https://doi.org/10.1021/bm500405h

75. Toh S, Tay J, Moy B, et al (2003) Size-effect on the physical characteristics of the aerobic granule in a SBR. Appl Microbiol Biotechnol 60:687–695. https://doi.org/10.1007/s00253-002-1145-y

76. Lin X, Wang Y (2017) Microstructure of anammox granules and mechanisms endowing their intensity revealed by microscopic inspection and rheometry. Water Research 120:22–31. https://doi.org/10.1016/j.watres.2017.04.053

77. Jia F, Yang Q, Liu X, et al (2017) Stratification of Extracellular Polymeric Substances (EPS) for Aggregated Anammox Microorganisms. Environ Sci Technol 51:3260–3268. https://doi.org/10.1021/acs.est.6b05761